



Bi₂S₃ for Aqueous Zn Ion Battery with Enhanced Cycle Stability

Cite as

Nano-Micro Lett.



(2020) 12:8


Received: 18 October 2019

Accepted: 29 November 2019

Published online: 19 December 2019

© The Author(s) 2019

Ting Xiong^{1,2}, Yinming Wang¹, Bosi Yin^{1,3}, Wen Shi¹, Wee Siang Vincent Lee¹ , Junmin Xue¹ 

 Wee Siang Vincent Lee, mseleew@nus.edu.sg; Junmin Xue, msexuejm@nus.edu.sg

¹ Department of Materials Science and Engineering, National University of Singapore, Singapore 117573, Singapore

² Centre for Advanced 2D Materials and Graphene Research Centre, National University of Singapore, Singapore 117546, Singapore

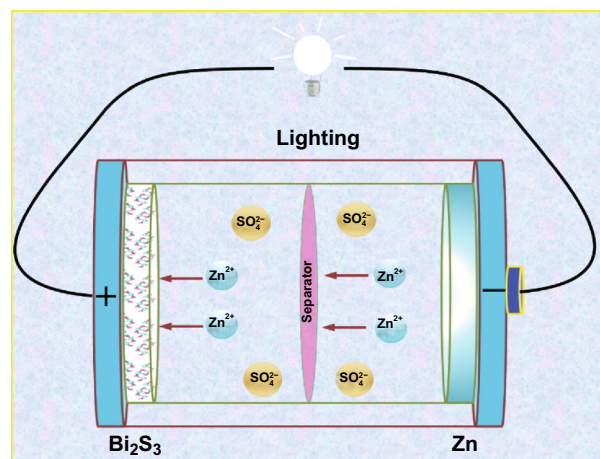
³ MIIT Key Laboratory of Critical Materials Technology for New Energy Conversion and Storage, School of Chemistry and Chemical Engineering, Harbin Institute of Technology, No. 92 West-Da Zhi Street, Harbin 150001, People's Republic of China

HIGHLIGHTS

- Bi₂S₃ is proposed as a promising cathode material for rechargeable aqueous Zn ion battery.
- The Zn/Bi₂S₃ battery shows a reversible capacity of 161 mAh g⁻¹ at 0.2 A g⁻¹ and good cyclic stability of up to 100 cycles with ca. 100% retention.
- The storage mechanism in the Bi₂S₃ cathode is related to the reversible Zn ion intercalation/extraction reactions and the capacitive contribution.

ABSTRACT Aqueous Zn ion batteries (ZIBs) are promising in energy storage due to the low cost, high safety, and material abundance. The development of metal oxides as the cathode for ZIBs is limited by the strong electrostatic forces between O²⁻ and Zn²⁺ which leads to poor cyclic stability. Herein, Bi₂S₃ is proposed as a promising cathode material for rechargeable aqueous ZIBs. Improved cyclic stability and fast diffusion of Zn²⁺ is observed. Also, the layered structure of Bi₂S₃ with the weak van der Waals interaction between layers offers paths for diffusion and occupancy of Zn²⁺. As a result, the Zn/Bi₂S₃ battery delivers high capacity of 161 mAh g⁻¹ at 0.2 A g⁻¹ and good cycling stability up to 100 cycles with ca. 100% retention. The battery also demonstrates good cyclic performance of ca. 80.3% over 2000 cycles at 1 A g⁻¹. The storage mechanism in the Bi₂S₃ cathode is related to the reversible Zn ion intercalation/extraction reactions and the capacitive contribution. This work indicates that Bi₂S₃ shows great potential as the cathode of ZIBs with good performance and stability.

KEYWORDS Aqueous; Zn ion battery; Bi₂S₃; Good stability



1 Introduction

Energy storage devices are in great demands for the integration of renewable energy and electrical energy infrastructures due to the energy crisis and environmental pollution [1–4]. Poised as the most successful commercial energy storage devices, lithium-ion batteries (LIB) are widely used due to their rechargeability and high energy density [5–7]. However, as the usage of LIB increases, there are growing concerns regarding the safety issues of flammable organic electrolytes and the availability of lithium resources [8, 9]. To reduce such heavy reliance on LIB, there is a renewed interest in alternative energy storage devices, especially those that utilize aqueous electrolyte, i.e., aqueous rechargeable battery (ARB) [10–13]. Among these ARBs, zinc ion batteries (ZIBs) are particularly attractive as zinc displays water compatibility, natural abundance, relatively low redox potential (-0.76 V vs. SHE) and high theoretical capacity (820 mAh g^{-1}) [14–16]. Despite these numerous advantages, cathode material selection is highly stringent which poses significant difficulties in developing advanced cathode materials that show both high energy density and long cycling stability.

The most widely studied ZIBs cathode materials remain to be metal oxides such as vanadium-based oxides and manganese-based oxides [17–21]. Despite many successful demonstrations of vanadium-based and manganese-based oxides in ZIBs application, one main concern for these materials is the presence of high negative charge density O^{2-} from $M-O$ where $M = Mn$ or V . Such concern is amplified for ZIBs as compared to LIB due to the shuttling of densely positive charged Zn^{2+} across the material which may lead to strong electrostatic forces between O^{2-} and Zn^{2+} [16, 22]. The strongly electrostatically “glued” Zn would then be unable to be fully removed during the charging process which could eventually lead to two major issues; (1) high initial irreversible loss, and (2) poor cyclic stability. While such an issue can be alleviated with the incorporation of structural water in the interlayer spacing as an electrostatic shield, alternative strategies remain scarce [23, 24]. An alternative strategy to minimize the impact of electrostatic “adhesion” of Zn^{2+} onto O^{2-} is to replace oxide in metal oxide with sulfide. Even though metal sulfides are less studied in ZIBs than metal oxide, the anion replacement from O^{2-} to S^{2-} may reduce

the tendency of these electrostatic “adhesion” and therefore leading to improved cyclic stability and minimizing the initial irreversible capacity loss [16, 22]. Furthermore, the lack in metal sulfide studies provides excellent explorative opportunities which could potentially lead toward the development of high-performing ZIBs cathode with high cyclic stability. While there are a few reports on metal sulfides for ZIBs application such as VS_2 [25], and this small material repertoire requires urgent expansion and further exploration. Bi_2S_3 is a semiconductor material with a narrow band gap of 1.3 eV, and high ionic conductivity which have attracted significant attention in electrochemistry application. In particular, the highly anisotropic Bi_4S_6 layers that are held together by weak van der Waals interaction provides sufficient pathway for foreign ions to intercalate into. As such, it has been studied as lithium-ion battery, and sodium ion battery cathodes [26, 27]. Such layered structure presents exciting opportunity for ion intercalation which may provide possible Zn^{2+} storage.

Hence, motivated by this phenomenon, Bi_2S_3 is investigated as ZIBs cathode in this work. Bi_2S_3 nanoparticles were synthesized using a facile chemical method followed by calcining. Bi_2S_3 with layered structure offers paths for fast diffusion and occupancy of Zn^{2+} , and also shows good cyclic stability. The as-prepared Bi_2S_3 delivers a high capacity of 161 mAh g^{-1} at a current density of 0.2 A g^{-1} and exhibits enhanced cyclic stability (100% retention after 100 cycles at 0.2 A g^{-1}) as the cathode for ZIBs. The energy storage mechanism of the Bi_2S_3 electrode is revealed by a series of measurements. Results demonstrate that the capacitive process and the intercalation/deintercalation of Zn^{2+} in the Bi_2S_3 interlayer occur during discharging/charging processes. Our finding shows that Bi_2S_3 is a promising cathode material with high capacity and good stability for the development of high-performance aqueous Zn ion battery system.

2 Experimental Section

2.1 Chemicals

Na_2S , $Bi(NO_3)_3 \cdot 5H_2O$, and $ZnSO_4 \cdot 7H_2O$ were purchased from Sigma-Aldrich. Acetic acid was purchased from Fluka. Carbon paper (0.18 mm, 77% porosity) was purchased from Ce-Tech Co. Ltd.

2.2 Synthesis of Bi₂S₃ Nanoparticles

Bi₂S₃ nanoparticles were synthesized by a simple chemical reaction followed by a simple calcining method. Typically, 0.97 g of Bi(NO₃)₃·5H₂O was dissolved into 100 mL H₂O containing 9 mL acetic acid. Then, 30 mL of Na₂S solution (0.003 mol) was added into the above solution and kept for stirring 2 h. The solid were collected by centrifugation, washed with ethanol and distilled water for three times, and then dried at 60 °C. The dried solid was then heat-treated in a vacuum oven at 200 °C for 3 h to yield crystallized Bi₂S₃ nanoparticles.

2.3 Characterization

The powder X-ray diffraction (XRD) pattern was measured by a powder diffractometer (Bruker D8 Advanced Diffractometer System) with a Cu K α (1.5418 Å) source. Scanning electron microscopy (SEM) images were recorded on a ZEISS SEM Supra 40 (5 kV). Transmission electron microscopy (TEM) was performed on a JEOL-3010 (300 kV acceleration voltage). TEM samples were prepared by dripping the sample solutions onto a copper grid. Surface composition was studied by X-ray photoelectron spectroscopy (XPS) using a Kratos Analytical Axis UltraDLD UHV spectrometer with a monochromatized Al K α X-ray source (1486.6 eV) scanning a spot size of 700 μ m by 300 μ m.

2.4 Electrochemical Measurements

All electrochemical tests were tested using an electrochemical station (Bio-logic VMP 3) at room temperature. A CR2025-type coin cell was constructed to evaluate the electrochemical performance. The as-prepared Bi₂S₃ nanoparticles were mixed with carbon black and polyvinyl difluoride in a 7:2:1 weight ratio with N-methyl-2-pyrrolidone. The mixture was hand-grinded and then coated onto the carbon paper, and finally dried at 80 °C for further use as cathode. Zn foil was used as the anode and filter paper was applied as the separator. 2 M of ZnSO₄ was employed as the electrolyte. For both cyclic voltammetry and charge/discharge tests, the voltage was measured in the range of 0.4–1.2 V. The current densities of 0.2, 0.3, 0.4, 0.5, 0.6, 0.8, 1, 2, 3, 4, 5, 6, 8, and 10 A g⁻¹ were selected for charge/discharge

test. Electrochemical impedance spectroscopy was tested in the frequency range from 0.01 to 10⁵ Hz. Specific capacity, energy density, and power density were determined using the mass of the active material from the cathode. The mass of the active material is about 1 mg, pasted onto a 1.2 cm in diameter carbon paper.

3 Results and Discussion

The Bi₂S₃ nanoparticles were synthesized via a simple chemical reaction followed by calcination. The XRD pattern of the obtained Bi₂S₃ nanoparticles displays a high degree of crystallization. All the diffraction peaks of the obtained sample can be indexed to orthorhombic Bi₂S₃ (JCPDS No. 17-0320) (Fig. 1a). The crystal structure of Bi₂S₃ is shown in Fig. 1b, which consisted of sheets of atoms parallel to the *z*-axis with each S surrounded by three Bi atoms and each Bi atom surrounded by three S atoms [28]. Also, sufficient interlayer spacing in the layers offers paths for diffusion and occupancy of foreign ions to storage energy. XPS spectrum in Fig. 1c confirms that the synthesized material is mainly composed of S and Bi elements (C and O signals come from the reference sample and absorbed oxygen).

TEM images show that the Bi₂S₃ exhibits nanoparticle-like morphology (Fig. 1d, e). The size of the nanoparticles is in the range of 10–50 nm, and the nanosized structure could suppress volume expansions during intercalation and deintercalation of ions [29]. The lattice distance of 0.503 nm corresponds to the (120) crystal plane of Bi₂S₃ in high-resolution TEM image (Fig. 1f). The SAED in the inset of Fig. 1f confirms the polycrystalline nature of the synthesized Bi₂S₃ nanoparticles. Further microstructural features of the synthesized Bi₂S₃ samples were investigated by N₂ adsorption–desorption isotherms as shown in Fig. S1a. The type IV isotherm (IUPAC definition) is obtained with a Brunauer–Emmett–Teller surface area of 16 m² g⁻¹, and the H1 hysteresis loop demonstrates the presence of mesopores [30]. The pore size distribution (Fig. S1b) shows the mesopores centered at 28 nm, formed by the aggregated nanoparticles. Originating from the high crystallinity, nanosized structure and mesopores, the synthesized Bi₂S₃ is expected to show good electrochemical performance.

The electrochemical performance of the material was assessed by assembling a Zn/Bi₂S₃ cell using Bi₂S₃ as

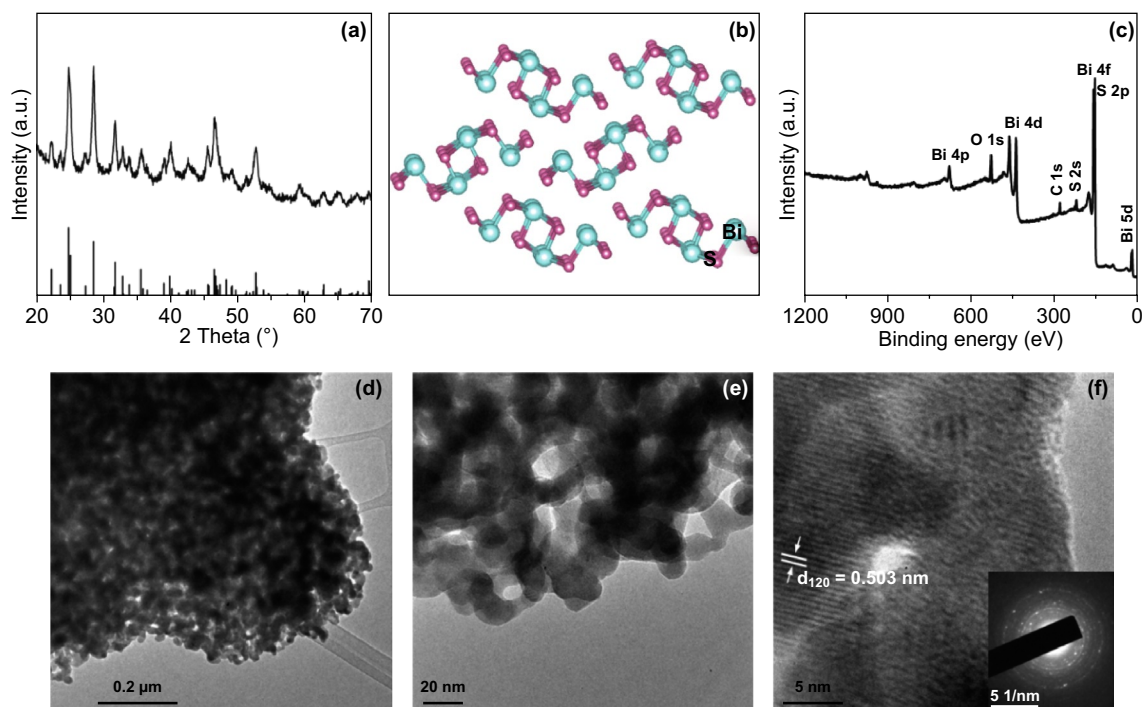


Fig. 1 **a** XRD pattern, **b** crystallographic structure, **c** XPS spectrum, **d**, **e** TEM images, and **f** High-resolution TEM image of Bi_2S_3 nanoparticles (inset of the SAED image)

cathode and Zn foil as anode in an aqueous solution of 2 M ZnSO_4 . Figure 2a shows the cyclic voltammetry (CV) curve of Zn/ Bi_2S_3 cell at scan rate of 0.5 mV s^{-1} in the voltage window of 0.4–1.2 V. Obvious redox peaks could be observed, which may be related to the interaction between Bi_2S_3 and Zn ions. In addition, galvanostatic discharge/charge (GCD) profiles are in accordance with the CV curves, which show one plateau around 0.6 V (Fig. 2b). Zn/ Bi_2S_3 cell shows a high discharge capacity of 161 mA h g^{-1} at 0.2 A g^{-1} . It also shows excellent rate performance, demonstrating high capacities of 143, 132, 121, 113, and 101 mAh g^{-1} at 0.3, 0.4, 0.5, 0.6, and 0.8 A g^{-1} , respectively (Fig. 2c).

The energy and power densities of the Zn/ Bi_2S_3 battery are calculated as shown in Fig. 2d. It can be seen that the assembled battery shows a maximum energy density of 105 Wh kg^{-1} , and also it delivers a maximum power density of 1455 W kg^{-1} . For the long-term cycling stability, the Zn/ Bi_2S_3 cell obtains a cyclic retention of 100% up to 100 cycles at a low current density of 0.2 A g^{-1} , with the corresponding coulombic efficiency approaching 100% (Fig. 2e). The capacity remains 80.3% after 2000 cycles

at current density of 1 A g^{-1} (Fig. 2f). Also, we tested the XRD of the cycled Bi_2S_3 , and the result shows that the sample is stable because it shows similar XRD pattern to the fresh one (Fig. S2). The good stability indicates that the Bi_2S_3 is a promising material for Zn ion battery application.

Electrochemical impedance spectroscopy (EIS) measurements are performed on the Zn/ Bi_2S_3 battery to study the detailed reaction kinetics. Figure 3a exhibits the Nyquist plots with a semicircle (at high frequency) involved with charge transfer and a sloped line associated with ion diffusion (at low frequency) [31]. In the equivalent circuit, by fitting, Bi_2S_3 shows low resistance of R_s (equivalent series resistance, $5.02 \text{ Oh}\Omega$), R_{CT} (charge transfer resistance, $4.1 \text{ Oh}\Omega$), and Z_W ($936.2 \text{ Oh}\Omega$), illustrating the fast reaction kinetics. The fast reaction kinetics could be attributed to the reduced electrostatic “adhesion” of Zn^{2+} onto anion S^{2-} which leads to fast diffusion of Zn^{2+} . To reveal the electrochemical kinetics of the Bi_2S_3 electrode, CV curves at different scan rates from 0.1 to 0.5 mV s^{-1} are studied in Fig. 3b. In each curve, three peaks were observed. An equation for analyzing the

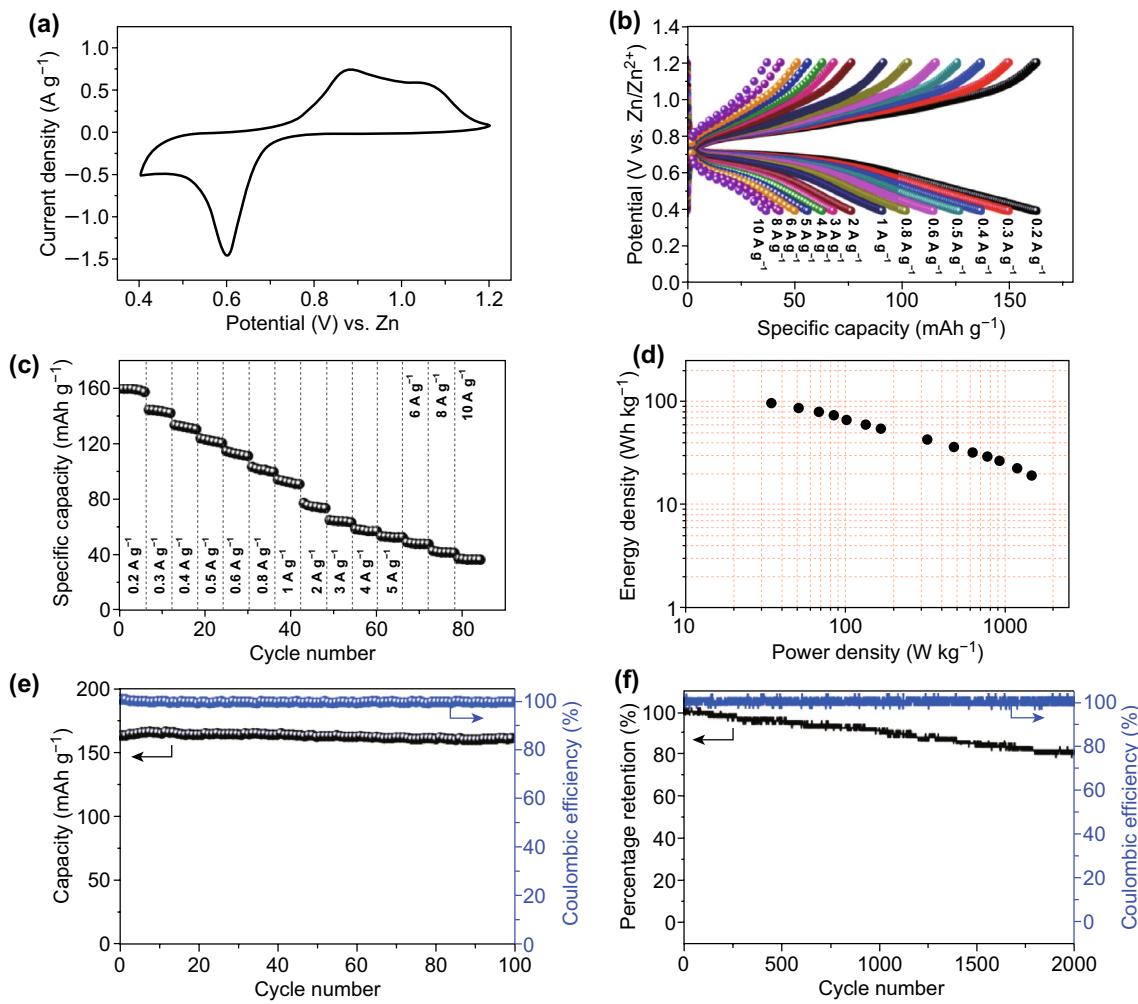


Fig. 2 **a** CV curve at 0.5 mV s^{-1} . **b** The charge/discharge curves. **c** Rate performance of Zn/Bi₂S₃ cell at current densities from 0.2 to 10 A g⁻¹. **d** Ragone plot. **e, f** The long-term cycling performance at current density of 0.2 A g⁻¹ and 1 A g⁻¹

electrochemical kinetics processes, based on the peak currents (i) and scan rates (v) is shown as Eq. 1 [32, 33]:

$$i = av^b \tag{1}$$

which can be equally written as Eq. 2

$$\log(i) = b \log(v) + \log(a) \tag{2}$$

where b is defined as the slope of $\log(i)$ versus $\log(v)$ curve. Typically, the value of b (0.5–1) is related to the type of electrochemical process. When b value reaches 0.5, it indicates that the electrochemical kinetics process is dominated by ionic diffusion. Surface capacitive effects become dominant as the b value is 1. From Fig. 3c, the b values for peak 1, 2, and 3 are determined to be 0.81, 0.91, and 0.97, separately. These b values hint that the ionic diffusion along with

surface capacitive effects would control the electrochemical kinetics reaction for Zn/Bi₂S₃ cell. The contribution from capacitor-like and diffusion-controlled processes can further be determined by Eq. 3 [34, 35]:

$$i = k_1v + k_2v^{1/2} \tag{3}$$

which can be rewritten in Eq. 4

$$i/v^{1/2} = k_1v^{1/2} + k_2 \tag{4}$$

where i is related to the total current response, k_1v represents current from surface capacitive effects, and $k_2v^{1/2}$ means current because of ionic diffusion process. As k_1 could be achieved via fitting $i/v^{1/2}$ versus $v^{1/2}$ plots, the contribution from capacitive effect is determined to be 86.5% at scan rate of 0.1 mV s^{-1} . As scan rate increases, the percentage

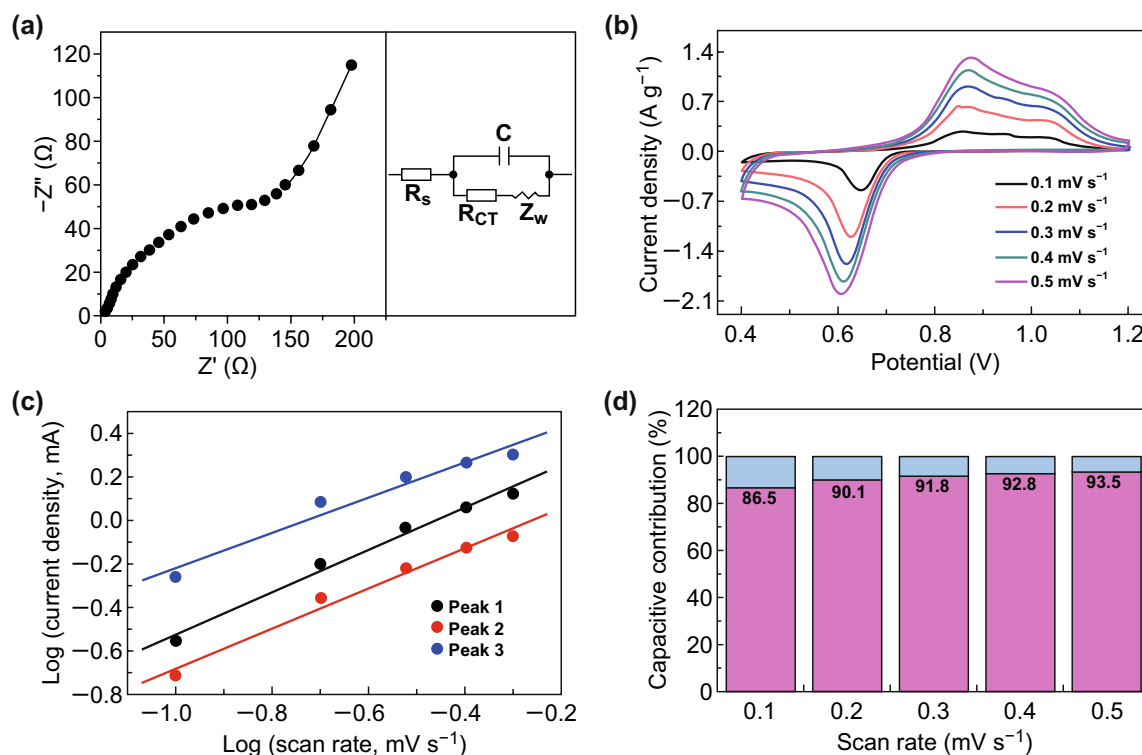


Fig. 3 **a** Electrochemical impedance spectroscopy (EIS). **b** CV curves at different scan rates. **c** The corresponding plots of log (peak current) versus log (scan rate) at the redox peaks. **d** The calculated capacitive contributions

of capacitive contribution is up to 90.1%, 91.8%, 92.8%, and 93.5% at 0.2, 0.3, 0.4, and 0.5 mV s^{-1} , respectively (Fig. 3d). The results suggest that the capacitive contribution is dominant, and the capacitive contribution ratios gradually increase with an increase in scan rate.

The storage mechanism is investigated by ex situ XRD, XPS spectra, SEM–EDX elemental mappings and TEM. Before charge/discharge process, we performed CV for 30 cycles to get a stable state. From the charge/discharge processes as shown in Fig. 4a, b, it indicates that $\text{ZnSO}_4 \cdot 3\text{Zn}(\text{OH})_2 \cdot 4\text{H}_2\text{O}$ (JCPDS No. 09-0204) is successively formed during the discharge process. Subsequently, $\text{ZnSO}_4 \cdot 3\text{Zn}(\text{OH})_2 \cdot 4\text{H}_2\text{O}$ disappears after being fully charged to 1.2 V. These results demonstrate the reversible formation/decomposition of $\text{ZnSO}_4 \cdot 3\text{Zn}(\text{OH})_2 \cdot 4\text{H}_2\text{O}$ during the discharge/charge process. The storage mechanism was also investigated by the XPS spectra at different charge/discharge states (Fig. 4c). It should be noted that a small amount of Zn^{2+} ions in Bi_2S_3 is detected after 30 cycles, suggesting that some of Zn^{2+} ions were trapped into Bi_2S_3 (state ① in Fig. 4c). During the discharging process, two pairs of Zn^{2+} peaks gradually appear at 1024.1/1047.1 eV

and 1024.8/1047.9 eV, which are attributed to the Zn^{2+} in $\text{Zn}(\text{OH})_2$ and ZnSO_4 from $\text{ZnSO}_4 \cdot 3\text{Zn}(\text{OH})_2 \cdot 4\text{H}_2\text{O}$, separately [19]. Meantime, the intensity about the Zn^{2+} peaks at 1023.3/1046.3 eV associated with the inserted Zn^{2+} in Bi_2S_3 increases, confirming the Zn^{2+} insertion process.

During the charging process, the peaks associated with the Zn^{2+} in $\text{Zn}(\text{OH})_2$ and ZnSO_4 from $\text{ZnSO}_4 \cdot 3\text{Zn}(\text{OH})_2 \cdot 4\text{H}_2\text{O}$ gradually disappear, further confirming the reversible conversion of $\text{ZnSO}_4 \cdot 3\text{Zn}(\text{OH})_2 \cdot 4\text{H}_2\text{O}$, consistent with the XRD result. Simultaneously, the peak intensity gradually decreases for the inserted Zn^{2+} in Bi_2S_3 . It indicates the continuous and reversible intercalation/extraction of Zn^{2+} in Bi_2S_3 during the electrochemical processes. SEM–EDX elemental mappings of the fully discharged Bi_2S_3 electrode are shown in Fig. S3. Obviously, elemental Zn is uniformly distributed in the Bi_2S_3 nanoparticles, which confirms the insertion mechanism of Zn ion into Bi_2S_3 layers.

The structural evolution of Bi_2S_3 electrode was further investigated by TEM analysis. For the Bi_2S_3 electrode at the fully discharged state, in Fig. 4d, e, nanoplates could be observed, and the observed lattice fringes with interplanar distances of ca. 1 nm correspond to the plane of

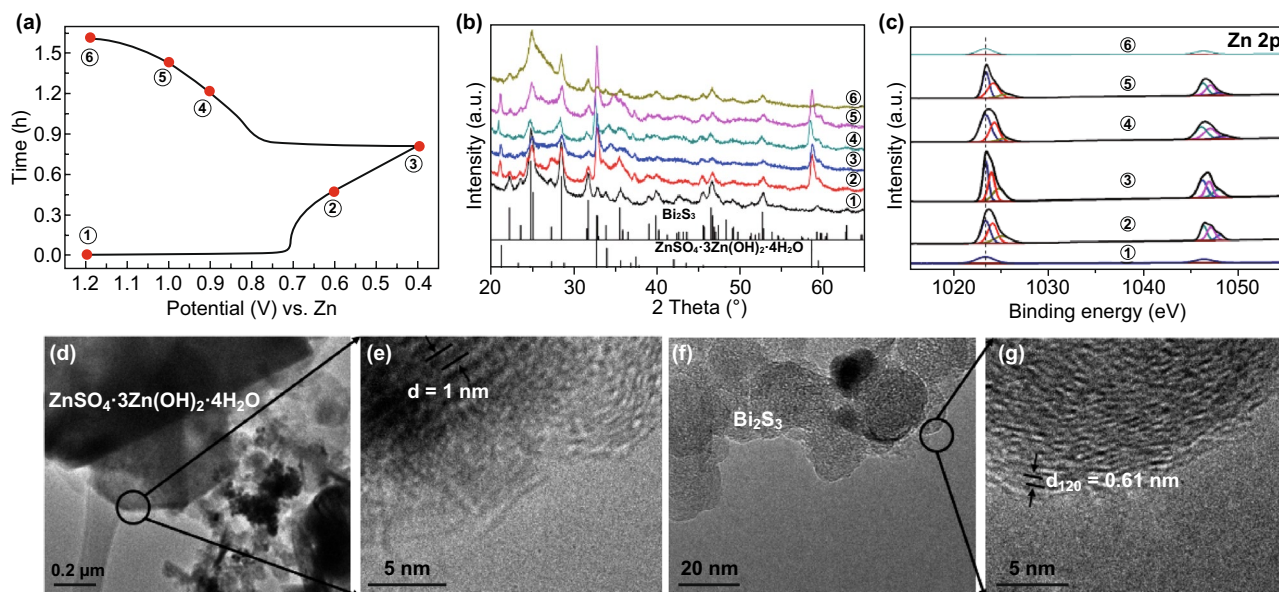


Fig. 4 **a** Charge/discharge curve at 0.2 A g^{-1} . **b** The corresponding ex situ XRD patterns. **c** XPS spectra Zn 2p at selected states. **d, e** TEM images of $\text{ZnSO}_4 \cdot 3\text{Zn(OH)}_2 \cdot 4\text{H}_2\text{O}$. **f, g** TEM images of Bi_2S_3 at the fully discharged state

$\text{ZnSO}_4 \cdot 3\text{Zn(OH)}_2 \cdot 4\text{H}_2\text{O}$, indicating the generation of $\text{ZnSO}_4 \cdot 3\text{Zn(OH)}_2 \cdot 4\text{H}_2\text{O}$ during the discharge process, consistent with the XRD and XPS analysis. Also, Bi_2S_3 with nanoparticles structure could be observed. The lattice spacing of 0.61 nm , which was enlarged when compared with that of the fresh Bi_2S_3 with lattice distance of 0.503 nm , was clearly observed in the HRTEM image (Fig. 4f, g). The enlarged lattice could be attributed to the insertion of Zn^{2+} . The layered structure of Bi_2S_3 with the weak van der Waals interaction between layers offers paths for diffusion and occupancy of Zn^{2+} .

Hence, based on the collective results, the electrochemical mechanism of $\text{Zn}/\text{Bi}_2\text{S}_3$ is related to the capacitive process and the intercalation/extraction of Zn^{2+} into the Bi_2S_3 framework during discharging/charging process, which is summarized as follows: During the discharge process, $\text{ZnSO}_4 \cdot 3\text{Zn(OH)}_2 \cdot 4\text{H}_2\text{O}$ is successively formed which is confirmed by the XRD, XPS (the detected Zn^{2+} peaks in Zn(OH)_2 and ZnSO_4 from $\text{ZnSO}_4 \cdot 3\text{Zn(OH)}_2 \cdot 4\text{H}_2\text{O}$) and TEM (the observed interplanar distances of ca. 1 nm for $\text{ZnSO}_4 \cdot 3\text{Zn(OH)}_2 \cdot 4\text{H}_2\text{O}$) results. Meantime, Zn^{2+} is inserted into Bi_2S_3 as revealed by the XPS (enhanced Zn^{2+} peaks intensity of the inserted Zn^{2+} in Bi_2S_3), TEM (enlarged lattice distance of 0.61 nm for Bi_2S_3), and SEM–EDX elemental mappings (uniform distribution of Zn^{2+} in the discharged Bi_2S_3) results. During the charging process,

$\text{ZnSO}_4 \cdot 3\text{Zn(OH)}_2 \cdot 4\text{H}_2\text{O}$ gradually disappears. These results demonstrate the reversible formation/decomposition of $\text{ZnSO}_4 \cdot 3\text{Zn(OH)}_2 \cdot 4\text{H}_2\text{O}$ during the discharge/charge process. At the same time, Zn^{2+} ions are extracted from Bi_2S_3 as demonstrated by the decreased XPS intensity of Zn^{2+} ions. Overall, the designed Bi_2S_3 electrode shows high zinc ion storage performance with faster reaction kinetics, higher capacity and better long-term cycles, presenting a potentially safe, durable, and low-cost device for large-scale energy storage.

4 Conclusions

In conclusion, we report a simple chemical method followed by calcining to synthesize Bi_2S_3 nanoparticles as cathodes for aqueous rechargeable ZIBs. The obtained Bi_2S_3 nanoparticles display high capacity of 161 mAh g^{-1} at current density of 0.2 A g^{-1} . Good rate behavior is demonstrated, and the $\text{Zn}/\text{Bi}_2\text{S}_3$ cells show good cycling stability over 100 cycles. At high current density of 1 A g^{-1} , the cell still keeps 80.3% retention after 2000 cycles. Mechanistic details of the Zn storage based on surface capacitive effects and Zn^{2+} ions insertion are demonstrated. The high capacity, good stability, and low cost make our battery promising for stationary energy storage applications.

Acknowledgements This work was supported by Singapore MOE Tier 1 funding R-284-000-162-114 and Singapore MOE Tier 2 MOE 2018-T2-1-149.

Open Access This article is licensed under a Creative Commons Attribution 4.0 International License, which permits use, sharing, adaptation, distribution and reproduction in any medium or format, as long as you give appropriate credit to the original author(s) and the source, provide a link to the Creative Commons licence, and indicate if changes were made. The images or other third party material in this article are included in the article's Creative Commons licence, unless indicated otherwise in a credit line to the material. If material is not included in the article's Creative Commons licence and your intended use is not permitted by statutory regulation or exceeds the permitted use, you will need to obtain permission directly from the copyright holder. To view a copy of this licence, visit <http://creativecommons.org/licenses/by/4.0/>.

Electronic supplementary material The online version of this article (<https://doi.org/10.1007/s40820-019-0352-3>) contains supplementary material, which is available to authorized users.

References

1. E. Karden, S. Ploumen, B. Fricke, T. Miller, K. Snyder, Energy storage devices for future hybrid electric vehicles. *J. Power Sources* **168**, 2–11 (2007). <https://doi.org/10.1016/j.jpowsour.2006.10.090>
2. X. Wang, X. Lu, B. Liu, D. Chen, Y. Tong, G. Shen, Flexible energy-storage devices: design consideration and recent progress. *Adv. Mater.* **26**, 4763–4782 (2014). <https://doi.org/10.1002/adma.201400910>
3. P. Yang, P. Sun, W. Mai, Electrochromic energy storage devices. *Mater. Today* **19**, 394–402 (2016). <https://doi.org/10.1016/j.mattod.2015.11.007>
4. J. Liu, J. Wang, C. Xu, H. Jiang, C. Li, L. Zhang, J. Lin, Z.X. Shen, Advanced energy storage devices: basic principles, analytical methods, and rational materials design. *Adv. Sci.* **5**, 1700322 (2018). <https://doi.org/10.1002/advs.201700322>
5. M. Yoshio, R.J. Brodd, A. Kozawa, *Lithium-Ion Batteries* (Springer, New York, 2008), pp. 1–452
6. H. Li, Z. Wang, L. Chen, X. Huang, Research on advanced materials for Li-ion batteries. *Adv. Mater.* **21**, 4593–4607 (2009). <https://doi.org/10.1002/adma.200901710>
7. N. Nitta, F. Wu, J.T. Lee, G. Yushin, Li-ion battery materials: present and future. *Mater. Today* **18**, 252–264 (2015). <https://doi.org/10.1016/j.mattod.2014.10.040>
8. J.B. Goodenough, Y. Kim, Challenges for rechargeable Li batteries. *Chem. Mater.* **22**, 587–603 (2010). <https://doi.org/10.1021/cm901452z>
9. V. Etacheri, R. Marom, R. Elazari, G. Salitra, D. Aurbach, Challenges in the development of advanced Li-ion batteries: a review. *Energy Environ. Sci.* **4**, 3243–3262 (2011). <https://doi.org/10.1039/C1EE01598B>
10. F. Beck, P. Rüetschi, Rechargeable batteries with aqueous electrolytes. *Electrochim. Acta* **45**, 2467–2482 (2000). [https://doi.org/10.1016/S0013-4686\(00\)00344-3](https://doi.org/10.1016/S0013-4686(00)00344-3)
11. D. Kundu, B.D. Adams, V. Duffort, S.H. Vajargah, L.F. Nazar, A high-capacity and long-life aqueous rechargeable zinc battery using a metal oxide intercalation cathode. *Nat. Energy* **1**, 16119 (2016). <https://doi.org/10.1038/nenergy.2016.119>
12. L. Chen, J.L. Bao, X. Dong, D.G. Truhlar, Y. Wang, C. Wang, Y. Xia, Aqueous Mg-ion battery based on polyimide anode and prussian blue cathode. *ACS Energy Lett.* **2**, 1115–1121 (2017). <https://doi.org/10.1021/acscenergylett.7b00040>
13. S.-W. Kim, D.-H. Seo, X. Ma, G. Ceder, K. Kang, Electrode materials for rechargeable sodium-ion batteries: potential alternatives to current lithium-ion batteries. *Adv. Energy Mater.* **2**, 710–721 (2012). <https://doi.org/10.1002/aenm.201200026>
14. C. Xu, B. Li, H. Du, F. Kang, Energetic zinc ion chemistry: the rechargeable zinc ion battery. *Angew. Chem. Int. Ed.* **51**, 933–935 (2012). <https://doi.org/10.1002/anie.201106307>
15. W. Xu, Y. Wang, Recent progress on zinc-ion rechargeable batteries. *Nano-Micro Lett.* **11**, 90 (2019). <https://doi.org/10.1007/s40820-019-0322-9>
16. G. Fang, J. Zhou, A. Pan, S. Liang, Recent advances in aqueous zinc-ion batteries. *ACS Energy Lett.* **310**, 2480–2501 (2018). <https://doi.org/10.1021/acscenergylett.8b01426>
17. H. Pan, Y. Shao, P. Yan, Y. Cheng, K.S. Han et al., Reversible aqueous zinc/manganese oxide energy storage from conversion reactions. *Nat. Energy* **1**, 16039 (2016). <https://doi.org/10.1038/nenergy.2016.39>
18. T. Xiong, Z.G. Yu, H. Wu, Y. Du, Q. Xie et al., Defect engineering of oxygen-deficient manganese oxide to achieve high-performing aqueous zinc ion battery. *Adv. Energy Mater.* **9**, 1803815 (2019). <https://doi.org/10.1002/aenm.201803815>
19. F. Wan, L. Zhang, X. Dai, X. Wang, Z. Niu, J. Chen, Aqueous rechargeable zinc/sodium vanadate batteries with enhanced performance from simultaneous insertion of dual carriers. *Nat. Commun.* **9**, 1656 (2018). <https://doi.org/10.1038/s41467-018-04060-8>
20. N. Zhang, Y. Dong, M. Jia, X. Bian, Y. Wang et al., Rechargeable aqueous Zn–V₂O₅ battery with high energy density and long cycle life. *ACS Energy Lett.* **36**, 1366–1372 (2018). <https://doi.org/10.1021/acscenergylett.8b00565>
21. N. Zhang, F. Cheng, Y. Liu, Q. Zhao, K. Lei, C. Chen, X. Liu, J. Chen, Cation-deficient spinel ZnMn₂O₄ cathode in Zn(CF₃SO₃)₂ electrolyte for rechargeable aqueous Zn-ion battery. *J. Am. Chem. Soc.* **138**, 12894 (2016). <https://doi.org/10.1021/jacs.6b05958>
22. L.X. Geng, G.C. Lv, X.B. Xing, J.C. Guo, Reversible electrochemical intercalation of aluminum in Mo₆S₈. *Chem. Mater.* **27**, 4926–4929 (2015). <https://doi.org/10.1021/acs.chemmater.5b01918>

23. J. Huang, Z. Wang, M. Hou, X. Dong, Y. Liu, Y. Wang, Y. Xia, Polyaniline-intercalated manganese dioxide nanolayers as a high-performance cathode material for an aqueous zinc-ion battery. *Nat. Commun.* **9**, 2906 (2018). <https://doi.org/10.1038/s41467-018-04949-4>
24. M. Yan, P. He, Y. Chen, S. Wang, Q. Wei et al., Water-lubricated intercalation in $V_2O_5 \cdot nH_2O$ for high-capacity and high-rate aqueous rechargeable zinc batteries. *Adv. Mater.* **30**, 1703725 (2018). <https://doi.org/10.1002/adma.201703725>
25. P. He, M. Yan, G. Zhang, R. Sun, L. Chen, Q. An, L. Ma, Layered VS_2 nanosheet-based aqueous Zn ion battery cathode. *Adv. Energy Mater.* **7**, 1601920 (2017). <https://doi.org/10.1002/aenm.201601920>
26. J. Ni, Y. Zhao, T. Liu, H. Zheng, L. Gao, C. Yan, L. Li, Strongly coupled Bi_2S_3 @CNT hybrids for robust lithium storage. *Adv. Energy Mater.* **4**, 1400798 (2014). <https://doi.org/10.1002/aenm.201400798>
27. H. Liang, J. Ni, L. Li, Bio-inspired engineering of Bi_2S_3 -PPy yolk-shell composite for highly durable lithium and sodium storage. *Nano Energy* **33**, 213–220 (2017). <https://doi.org/10.1016/j.nanoen.2017.01.033>
28. S.-Q. Zhan, H. Wan, L. Xu, W.-Q. Huang, G.-F. Huang, J.-P. Long, P. Peng, Native vacancy defects in bismuth sulfide. *Int. J. Mod. Phys. B* **28**, 1450150 (2014). <https://doi.org/10.1142/S0217979214501501>
29. G. Qin, H. Zhang, C. Wang, Ultrasmall TiO_2 nanoparticles embedded in nitrogen doped porous graphene for high rate and long life lithium ion batteries. *J. Power Sources* **272**, 491–500 (2014). <https://doi.org/10.1016/j.jpowsour.2014.08.105>
30. K.S.W. Sing, D.H. Everett, R.A.W. Haul, L. Moscou, R.A. Pierotti, J. Rouquerol, T. Siemieniowska, Reporting physisorption data for gas/solid systems with special reference to the determination of surface area and porosity. *Pure Appl. Chem.* **57**, 603 (1985). <https://doi.org/10.1351/pac198557040603>
31. T. Xiong, Z.G. Yu, W.S.V. Lee, J. Xue, o-Benzenediol-functionalized carbon nanosheets as low self-discharge aqueous supercapacitors. *ChemSuschem* **11**, 3307–3314 (2018). <https://doi.org/10.1002/cssc.201801076>
32. K. Zhang, M. Park, L. Zhou, G.-H. Lee, W. Li, Y.-M. Kang, J. Chen, Urchin-like $CoSe_2$ as a high-performance anode material for sodium-ion batteries. *Adv. Funct. Mater.* **26**, 6728–6735 (2016). <https://doi.org/10.1002/adfm.201602608>
33. D. Chao, C. Zhu, P. Yang, X. Xia, J. Liu et al., Array of nanosheets render ultrafast and high-capacity Na-ion storage by tunable pseudocapacitance. *Nat. Commun.* **7**, 12122 (2016). <https://doi.org/10.1038/ncomms12122>
34. D. Chao, P. Liang, Z. Chen, L. Bai, H. Shen et al., Pseudocapacitive Na-ion storage boosts high rate and areal capacity of self-branched 2D layered metal chalcogenide nanoarrays. *ACS Nano* **10**, 10211–10219 (2016). <https://doi.org/10.1021/acsnano.6b05566>
35. X. Xia, D. Chao, Y. Zhang, J. Zhan, Y. Zhong et al., Generic synthesis of carbon nanotube branches on metal oxide arrays exhibiting stable high-rate and long-cycle sodium-ion storage. *Small* **2**, 3048–3058 (2016). <https://doi.org/10.1002/smll.201600633>

